

TinyDef-DETR: A DETR-based Framework for Defect Detection in Transmission Lines from UAV Imagery

Jiaming Cui ¹ , Shuai Zhou ² and Feng Shen ^{1*}

¹ Harbin Institute of Technology, Harbin 150001, China; hitcjm@outlook.com

² Electric Power Research Institute, Yunnan Power Grid Co., Ltd., Kunming 650217, China;

* Correspondence: fshen@hit.edu.cn (F.S.)

Abstract: Automated defect detection from UAV imagery of transmission lines is a challenging task due to the small size, ambiguity, and complex backgrounds of defects. This paper proposes TinyDef-DETR, a DETR-based framework designed to achieve accurate and efficient detection of transmission line defects from UAV-acquired images. The model integrates four major components: an edge-enhanced ResNet backbone to strengthen boundary-sensitive representations, a stride-free space-to-depth module to enable detail-preserving downsampling, a cross-stage dual-domain multi-scale attention mechanism to jointly model global context and local cues, and a Focaler-Wise-SIoU regression loss to improve the localization of small and difficult targets. Together, these designs effectively mitigate the limitations of conventional detectors. Extensive experiments on both public and real-world datasets demonstrate that TinyDef-DETR achieves superior detection performance and strong generalization capability, while maintaining modest computational overhead. The accuracy and efficiency of TinyDef-DETR make it a suitable method for UAV-based transmission line defect detection, particularly in scenarios involving small and ambiguous targets.

Keywords: Transmission lines; Defect detection; UAV imagery; Power industry; Transformer-based detectors

1. INTRODUCTION

Along with the sustained development of the Chinese economy, the mileage of transmission lines has increased rapidly[1]. As the core infrastructure for long-distance energy transmission, their reliable operation is essential for meeting the growing demand for electricity[2]. However, transmission lines are exposed to harsh outdoor environments[3], where prolonged exposure significantly raises the risk of diverse faults—ranging from component damage to foreign object intrusions—collectively referred to as transmission line defects[4].

Unmanned aerial vehicles (UAVs) are increasingly employed to capture imagery of transmission lines for post-flight visual inspection and defect detection[5]. In such UAV-acquired imagery, defects often appear as small objects due to long shooting distances and the inherent resolution limitations of aerial imaging systems[6]. These small targets typically occupy regions smaller than 32×32 pixels, lacking clear contours and distinct textures, which severely hampers reliable recognition[7]. The challenge is further exacerbated by complex backgrounds such as vegetation, towers, and shadows, where small defects are frequently obscured or confused with surrounding structures[8].

With the rapid advancement of smart grid development, transmission line defect detection has increasingly adopted deep learning-based object detection methods[9]. Alongside

Received:

Revised:

Accepted:

Published:

Citation: Lastname, F.; Lastname, F.; Lastname, F. Title. *Remote Sens.* **2025**, *1*, 0. <https://doi.org/>

Copyright: © 2025 by the authors. Submitted to *Remote Sens.* for possible open access publication under the terms and conditions of the Creative Commons Attribution (CC BY) license (<https://creativecommons.org/licenses/by/4.0/>).

arXiv:2509.06035v3 [cs.CV] 15 Sep 2025

this progress, numerous general-purpose detectors—such as YOLO[10], DINO[11], and RT-DETR[12]—have been developed. While these models achieve remarkable success in generic scenarios, most of them on the COCO dataset[13], they face notable limitations in transmission line defect detection under complex conditions involving occlusion, background clutter, and variable lighting[14]. Common issues include missed detections, false positives, and false negatives, which substantially undermine the practical utility of UAV-acquired imagery in real-world transmission line maintenance[15]. These shortcomings are consistently reported in previous studies and further confirmed by our preliminary experiments, highlighting the critical need for specialized detection frameworks capable of accurately identifying small-scale defects in UAV operational scenarios.

In this article, we propose TinyDef-DETR, a novel transmission line defect detection network built upon the Transformer[11] architecture, which aims to enhance detection accuracy, recall, and robustness for UAV-acquired imagery under complex inspection scenarios. The main contributions of this work are summarized as follows:

1. We construct an Edge Enhanced ResNet (EE-ResNet) by embedding an Edge-Enhanced Convolution (EEConv) module into the residual backbone. The EEConv integrates central, horizontal, and vertical difference convolutions to encode gradient priors, thereby improving sensitivity to fine-grained details and object boundaries. Through a re-parameterization strategy, the multi-branch structure of EEConv is fused into a single 3×3 kernel at inference, incurring no additional computational overhead. By augmenting the ResNet backbone with such edge-aware feature extraction, EE-ResNet substantially strengthens the representation capability for small-scale defects in UAV inspection imagery.
2. We introduce a stride-free downsampling module based on space-to-depth transformation, which reorganizes spatial information into the channel dimension using a fixed 2×2 partition without stride convolution. This design preserves pixel-level details while reducing spatial resolution, thereby improving recall for extremely small defects that are often missed by conventional strided convolution architectures.
3. We propose a lightweight attention block with a dual-domain Frequency–Channel–Spatial Aggregation (FCSA) mechanism, integrated in a cross-stage partial manner. This design jointly enhances global semantic reasoning and local detail preservation, enabling the network to better capture anisotropic defect patterns such as missing bolts, loose clamps, and sagging wires.
4. We develop a novel Focaler-Wise-SIoU loss that combines normalized IoU scaling, Scylla-IoU geometric penalties, and non-monotonic focal modulation. This adaptively emphasizes moderately difficult samples while suppressing trivial or noisy ones, thereby stabilizing training and improving localization accuracy for small-scale defect regions.

2. Related Works

2.1. Applications of CNN-based Model in Power Line Defect Detection

Yang et al. [16] proposed DRA-Net, a dual-branch residual attention CNN-based model for pixel-wise power line detection, incorporating residual and attention modules to enhance feature representation, which significantly improved detection accuracy; however, its performance still degrades in extremely complex backgrounds due to the model's limited ability to generalize across highly cluttered scenes. Liu et al. [17] proposed the Box-Point Detector, a CNN-based insulator fault diagnosis method that integrates object detection and keypoint localization to improve the precision of defect identification in aerial imagery, achieving high detection accuracy and robustness; however, its reliance on manual feature labeling and limited evaluation on diverse environmental conditions may constrain its

scalability and generalization in large-scale power line inspections. Yu et al.[18] developed RcpVGG-YOLOv5, a lightweight YOLOv5-based insulator defect detection algorithm that integrates noise reduction and target detection to enhance robustness in complex aerial backgrounds, achieving strong engineering applicability with reduced false detections; however, its lack of dedicated small-target detection strategies and the limited dataset size constrained accuracy to below 80%, indicating room for improvement in generalization and precision. Zhang et al.[19] introduced FAFNet, a CNN-based model incorporating feature alignment and multi-scale feature fusion to detect overhead transmission line components, which significantly enhanced detection accuracy and robustness; however, the method still faces limitations in handling small or heavily occluded targets, primarily due to the insufficient feature representation capability under extreme visual conditions. Zhang et al.[20] developed InsuDet, a CNN-based fault detection model for insulators in overhead transmission lines, integrating feature enhancement and region proposal improvements to achieve higher detection accuracy; nevertheless, its performance deteriorates under severe occlusion and complex backgrounds, mainly due to the insufficient robustness of feature extraction in highly cluttered environments. Tunio et al.[21] proposed a CNN-based model for fault detection and classification in overhead transmission lines, integrating comprehensive feature extraction and optimization strategies to enhance accuracy, which achieved superior classification performance; however, the model still struggles with generalization under highly variable fault conditions, primarily due to the limited adaptability of extracted features to unseen scenarios.

2.2. Applications of Transformer-Based Model in Power Line Defect Detection

Tian et al.[22] addressed the challenge of insulator defect detection in low-quality UAV imagery by introducing a patch-based diffusion model for image restoration and an optimized DETR with Spatial Information Interaction and Feature Convergence Modules, achieving superior detection accuracy of 95.8% particularly for small defects, while the limitations lie in incomplete coverage of defect types, restricted generalization across diverse grid structures, and computational inefficiency in real-time applications, primarily due to dataset constraints and model complexity. Cheng and Liu successively advanced Transformer-based approaches for insulator defect detection by first enhancing DETR[23] with refined attention and feature optimization to improve localization accuracy over the baseline, and later proposing AdIn-DETR[3] with lightweight feature fusion and task-specific adaptation for real-time end-to-end detection, achieving superior precision–efficiency trade-offs, though both methods remain limited by reduced robustness under complex backgrounds and unseen categories, largely due to dataset insufficiency and the inherent constraints of Transformer complexity and speed. Wang et al.[24] developed a Transformer-based detection framework for advanced insulator defect identification, integrating multi-scale feature enhancement and context-aware attention to improve recognition accuracy and robustness, achieving state-of-the-art reliability in complex grid environments, while the model still suffers from efficiency limitations and reduced adaptability to rare defect patterns, mainly due to computational overhead and the scarcity of diverse annotated datasets. Xie et al.[25] proposed Power-DETR, a Transformer-based end-to-end detection framework for power line defect components, in which contrastive denoising learning and a hybrid query selection strategy were introduced to enhance small-object recognition and detection robustness, achieving superior accuracy over baseline DETR, yet the method still faces challenges in computational efficiency and generalization to highly variable field conditions, mainly due to increased model complexity and limited dataset diversity. Yang and Wang [4] proposed a hybrid detection framework combining YOLOv5 with Transformer-based DETR to recognize bird nests on transmission lines from

small-sample datasets, introducing transfer learning and data augmentation to mitigate limited training data, which achieved reliable detection performance under constrained scenarios, while its limitation lies in reduced scalability and robustness for large-scale deployments, mainly due to dataset scarcity and the trade-off between lightweight training and generalization capacity.

3. Materials and Methods

3.1. Overview

In this study, we employ RE-DETR-r18[12] as the baseline detection framework owing to its superior accuracy and robustness in complex scenarios. Traditional DETR models often suffer from slow convergence and substantial computational overhead, which hinder their deployment in UAV-based inspection tasks.

Addressing these inherent limitations, RE-DETR incorporates an enhanced encoder–decoder architecture together with refined query interaction mechanisms, while for the backbone network, RT-DETR-r18 adopts a CNN-based design, namely the popular ResNet-18[26]. From the perspective of real-time performance, employing a CNN architecture for feature extraction further enhances the real-time capability of DETR-like models, thereby improving their practical applicability. As a result, RE-DETR not only accelerates convergence and improves detection precision, but also preserves the global context modeling capability of Transformer-based frameworks[11]. In addition, its lightweight optimization strategies—specifically, the design choice to apply the encoder only to high-level semantic features (S5) with relatively small spatial dimensions—effectively reduce resource consumption. This balances performance and speed by significantly decreasing computational overhead and accelerating inference without compromising accuracy, thereby making RE-DETR particularly suitable for post-flight UAV imagery analysis, where large volumes of data must be processed efficiently under computational and energy constraints[22].

By contrast, YOLO-based detectors, though widely favored for their real-time efficiency and ease of deployment[27], tend to degrade in performance when handling small, occluded, or densely distributed objects, owing to their anchor-dependent design and limited global receptive field. This aligns with the findings of Ismail et al.[28], who reported that while YOLO excels in real-time scenarios, it struggles with small-object detection and occlusion, whereas DETR achieves higher accuracy in complex environments at the cost of greater computational demand. Our preliminary experiments further compared RT-DETR with representative YOLO series models, including YOLOv3[29], YOLOv7[30], and YOLO 11[31], and showed that RT-DETR consistently outperformed most of them in overall performance. In cases where certain YOLO variants (e.g., YOLO 11m) surpassed RT-DETR, their gains were typically accompanied by substantially larger parameter sizes, thereby underscoring RT-DETR’s advantageous balance between model complexity and detection accuracy.

Taken together, the consistent advantages of RT-DETR over both traditional DETR models and representative YOLO series substantiate its adoption as the baseline framework in this study.

Building upon this strong foundation, we propose TinyDef-DETR as a dedicated solution for small object defect detection in UAV-based transmission line inspection. The overall architecture is illustrated in Fig.1.

First, the backbone adopts the Edge-Enhanced ResNet (EE-ResNet) structure to strengthen low-level detail preservation. Second, a compact Space-to-Depth Convolution (S2DConv) module is inserted before each downsampling layer to reorganize spatial features in a manner that preserves critical spatial information while reducing resolution, thereby improving the recall rate of extremely small objects. Third, a lightweight

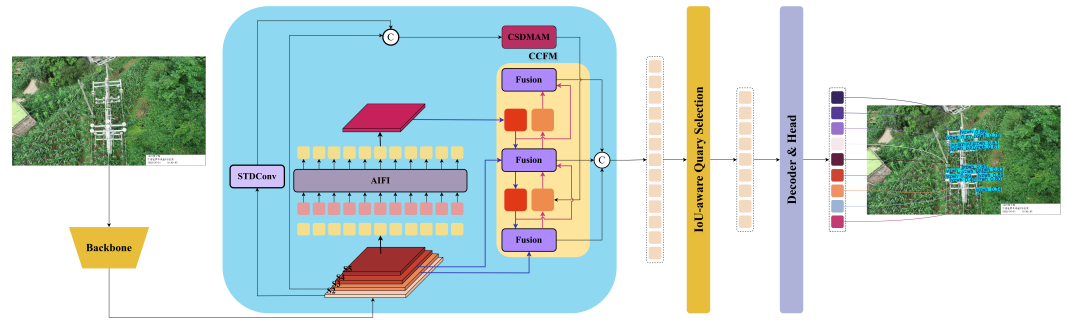


Figure 1. Overall framework of TinyDef-DETR

Cross-Stage Dual-Domain Multi-Scale Attention Module (CSDMAM) is embedded into the backbone network to enhance directional sensitivity and fine-grained structural modeling, effectively capturing anisotropic features of typical defects such as missing bolts, loose clamps, or sagging wires. Finally, a Focaler-Wise-SIoU loss function is employed to jointly optimize classification and localization. This loss function adaptively balances easy and hard samples while providing more accurate bounding box regression through shape-aware optimization, which further improves detection robustness for small and ambiguous targets. Detailed descriptions of the proposed modules can be found in Sections 3.2 to 3.5.

3.2. Edge Enhanced ResNet

ResNet[26] represents a milestone in deep learning for computer vision, introducing residual learning that enables the effective training of very deep networks. Owing to its simple yet modular design, it has become a widely adopted backbone across a broad spectrum of vision tasks. Nevertheless, when applied to UAV-based visual inspection for transmission line defect detection, native ResNet architectures, as verified in preliminary experiments, exhibit limited capability in capturing sufficiently fine-grained features, thereby constraining their effectiveness in identifying small and subtle defect targets, particularly in challenging transmission line inspection environments with interference from vegetation, man-made structures, and adjacent electrical installations.

Inspection of the heatmaps exported from ResNet further reveals that they lack clear edges and fine contours, which exacerbates the difficulty of accurately localizing subtle defects. Unlike conventional convolution, where the high performance of CNN-based edge feature extraction typically relies on large pretrained backbones—resulting in high memory consumption and energy cost, which contradicts the real-time requirements of UAV-based transmission line defect detection tasks—difference convolution introduces differential operations to enhance sensitivity to gradient variations and fine-grained structural details, thereby improving the extraction of local details and object boundaries[32].

To address the aforementioned problem, we propose an EEConv (edge enhancement convolution). Building on this idea, EEConv explicitly incorporates three difference convolution operators—central difference convolution (CDC), horizontal difference convolution (HDC), and vertical difference convolution (VDC)—to embed gradient priors into the feature extraction process. The overall structure of EEConv is illustrated in Fig. 2(a). To ensure deployment efficiency, EEConv adopts a re-parameterization strategy that fuses its multi-branch convolutions into a single equivalent 3×3 kernel during inference. Once fused, the auxiliary branches are discarded, leaving only a lightweight standard convolution. This allows the module to preserve the expressive power gained from multi-branch training while maintaining the same computational cost as a vanilla convolution. During deployment, the structure of EEConv becomes as shown in Fig. 2(b).

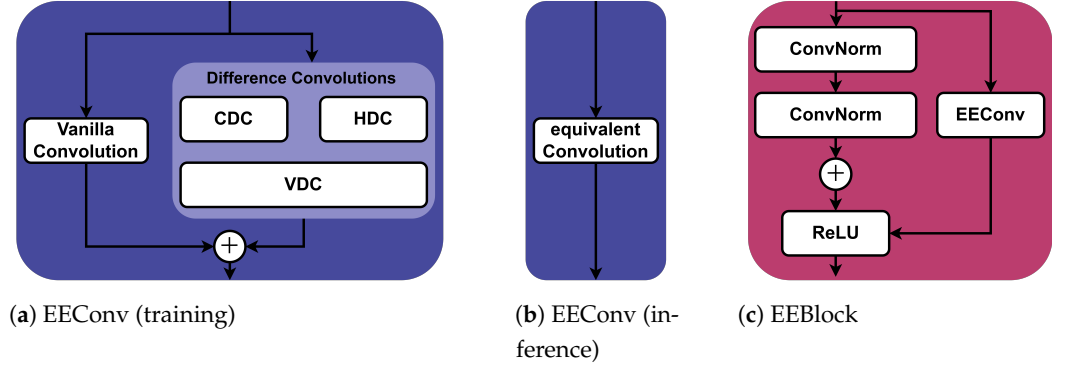


Figure 2. The architecture of EEBlock (Edge Enhanced Block)

Formally, let the three convolutional branches be denoted as (W_k, b_k) , $k = 1, \dots, 4$, corresponding to CDC, HDC, VDC and the conventional convolution, respectively. During training, their weights and biases are linearly combined:

$$W_{\Sigma} = \sum_{k=1}^3 W_k, \quad (1)$$

$$b_{\Sigma} = \sum_{k=1}^3 b_k. \quad (2)$$

The intermediate feature map is then obtained as

$$z = \text{Conv}_{3 \times 3}(x; W_{\Sigma}, b_{\Sigma}),$$

followed by batch normalization and a non-linear activation $\phi(\cdot)$:

$$y = \phi\left(\gamma \cdot \frac{z - \mu}{\sqrt{\sigma^2 + \epsilon}} + \beta\right).$$

For inference, the BN parameters are absorbed into the convolution kernel, yielding per-channel scaling:

$$\alpha_c = \frac{\gamma_c}{\sqrt{\sigma_c^2 + \epsilon}},$$

and the final equivalent kernel and bias are computed as

$$W_c^{(\text{final})} = \alpha_c \cdot W_{\Sigma, c}, \quad (3)$$

$$b_c^{(\text{final})} = \alpha_c \cdot (b_{\Sigma, c} - \mu_c) + \beta_c. \quad (4)$$

Thus, during deployment, EEConv degenerates into a single 3×3 convolution followed by activation:

$$y = \phi\left(\text{Conv}_{3 \times 3}(x; W^{(\text{final})}, b^{(\text{final})})\right),$$

which guarantees equivalence with the training-time formulation while ensuring zero additional inference overhead.

To integrate this into our framework, we replace the second 3×3 convolution in the residual branch of standard ResNet basic blocks with EEConv, thereby preserving the backbone's modular design while substantially improving sensitivity to fine-grained structures. This design choice is motivated by the observation that the second 3×3

convolution in each residual block primarily functions as a feature refiner, responsible for aggregating local structural details after the first convolution has extracted preliminary features. In this way, we obtain the Edge-Enhanced Block (EEBlock), whose structure is illustrated in Fig. 2(c).

By substituting the refining convolution with EEConv, we embed directional gradient priors precisely at the stage where fine-grained information is consolidated, thus maximizing the impact of EEConv on enhancing edge and detail representation. Meanwhile, the first 3×3 convolution and the shortcut connection remain unchanged, ensuring full compatibility with the original ResNet architecture and preserving its residual learning mechanism.

Integrating EEBlocks throughout the backbone yields the Edge-Enhanced ResNet (EE-ResNet), which significantly improves sensitivity to subtle structural details while maintaining computational efficiency. EE-ResNet provides a robust feature extraction foundation, offering stronger boundary-aware representations and improved resilience against background interference. This enhanced backbone design directly addresses the core challenge of detecting small-scale and fine-grained defects in transmission line imagery, thereby serving as a crucial cornerstone for the subsequent TinyDef-DETR framework. The overall architecture of the proposed EE-ResNet is illustrated in Fig. 3.

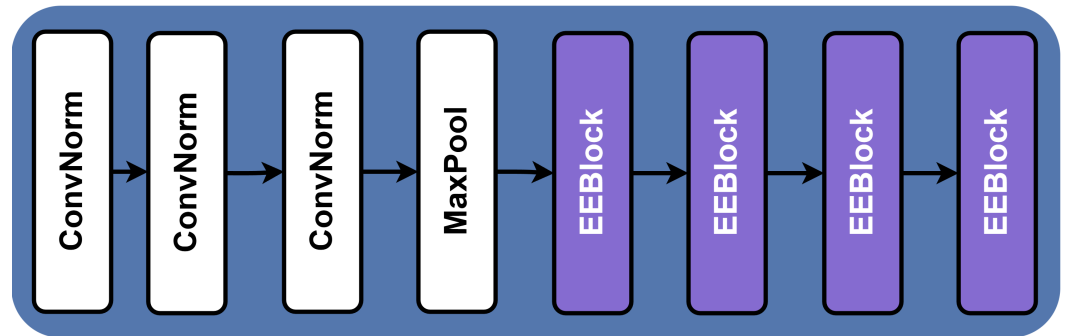


Figure 3. Overall framework of EE-ResNet

3.3. Space-to-depth Convolution

3.3.1. Principle of SPD(Space-to-depth Convolution)

Given the nature of transmission line defect detection—where the dataset is predominantly composed of small objects—preserving fine-grained information, maintaining balanced feature weighting, and performing effective feature representation learning contribute to improving both accuracy and recall [2].

During an extensive review of the literature, we came across the work of Sunkara and Luo [33], who pointed out that conventional CNN architectures exhibit an inherent limitation, namely the use of strided convolution. They emphasized that such designs inevitably lead to the loss of fine-grained information and result in less effective feature representations, which is particularly detrimental for low-resolution images and small object detection. This explains why conventional CNN-based approaches often fail to meet the requirements of small object detection, where the preservation of subtle spatial details is crucial.

Inspired by their findings, we incorporate the SPD(Space-to-depth Convolution) module into our proposed TinyDef-DETR framework. SPD adopts a stride-free downsampling strategy that redistributes pixels along the channel axis instead of discarding them, thereby preserving pixel-level information while reducing spatial resolution. In this way, TinyDef-DETR achieves more effective feature representations, improving both accuracy and recall for transmission line defect detection.

The SPD operation is defined on an input feature map

$$X \in \mathbb{R}^{S \times S \times C},$$

where S denotes the spatial resolution and C is the channel dimension. The goal is to downsample the spatial resolution by a factor of $scale$ while preserving all pixel-level information. Unlike conventional strided convolution that inevitably discards part of the input, SPD achieves lossless downsampling by spatial-to-channel rearrangement. Formally, the output feature map is given by

$$X' \in \mathbb{R}^{\frac{S}{scale} \times \frac{S}{scale} \times (C \cdot scale^2)}.$$

This transformation can be expressed as a structured partitioning of X . Specifically, for each spatial position (u, v) in X' , its corresponding feature vector is constructed by concatenating the values of X sampled from the $scale \times scale$ local neighborhood in the original feature map:

$$X'(u, v, :) = \bigoplus_{i=0}^{scale-1} \bigoplus_{j=0}^{scale-1} X(u \cdot scale + i, v \cdot scale + j, :)$$

where \bigoplus denotes concatenation along the channel dimension. In this way, all pixels from X are preserved in X' , but redistributed from the spatial dimensions into the channel dimension.

After the SPD transformation, the spatial resolution of the feature map is reduced by a factor of $scale$, while all pixel-level information is preserved through spatial-to-channel rearrangement. Consequently, the number of channels increases by a factor of $scale^2$. To further process this rearranged representation, a subsequent convolution layer is applied, which can be formally expressed as

$$X'' = f_{Conv}(X'; \mathbf{W}, \mathbf{b}), \quad X'' \in \mathbb{R}^{\frac{S}{scale} \times \frac{S}{scale} \times C_2},$$

where \mathbf{W} and \mathbf{b} denote the convolutional kernel weights and bias, respectively. This convolution simultaneously fuses information across the expanded channel dimension and adjusts it to the target dimension C_2 . In this way, the operation not only regulates the channel dimensionality but also enhances local feature representation through the structured partitioning.

An illustrative example of the SPDConv operation is presented in Fig.4.

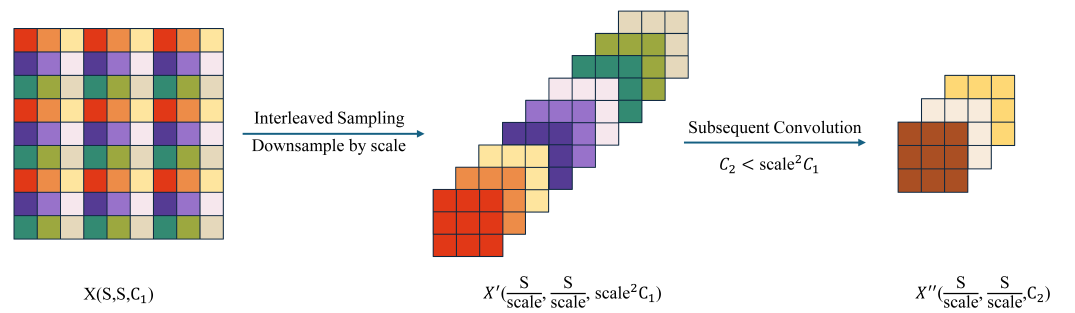


Figure 4. Illustration of SPDConv (Space-to-Depth Convolution)

3.3.2. Choice of the Downsampling Factor

A critical design decision in the SPD module is the choice of the downsampling factor *scale*.

Constraint of Small Object Size. In our dataset, small targets including polluted insulator, missing tie wire, and bird nest frequently span only $8 \sim 32$ pixels in the original image. If $scale = 4$ (or larger) were adopted, the smallest objects would be reduced to merely $2 \sim 8$ pixels at the first feature level. After further downsampling by the backbone and feature pyramid, these objects would rapidly degenerate into near-point responses, severely hindering recall. By contrast, $scale = 2$ preserves the effective resolution of small targets at the $4 \sim 16$ pixel level, which can still be robustly captured and aggregated by local 3×3 operators.

Compatibility with Detector Stride Hierarchy. Unlike many mainstream detectors that organize feature pyramids with strides $\{4, 8, 16, \dots\}$, our Edge Enhanced ResNet employs stage-wise downsampling with $stride = 2$. Consequently, setting SPD $scale = 2$ is equivalent to a lossless stride-2 operation, perfectly aligned with the subsequent stride-2 downsampling in the backbone/pyramid, preserving high-resolution shallow features crucial for small objects. In contrast, starting with $scale = 4$ effectively performs a stride-4 rearrangement at the outset, over-compressing shallow maps and weakening the small-object modeling capacity of early pyramid levels.

Anti-Aliasing and Information Fidelity. With $scale = 2$, the neighborhood is completely mapped into the channel dimension, ensuring that no samples are discarded. Although $scale \geq 4$ also performs rearrangement, the resulting features must be processed at a much lower spatial resolution, reducing the discriminability of local topology and diminishing the effective anti-aliasing capability.

Efficiency in Computation and Memory. After SPD, the channel dimension increases by a factor of $scale^2$. When $scale = 2$, channels are quadrupled while spatial dimensions are reduced by one quarter. As a result, the computational cost of the following 3×3 convolution remains comparable to that of a standard stride-2 convolution, but without discarding information. In contrast, $scale = 4$ would increase the channel dimension by sixteen while reducing spatial size by one sixteenth, leading to heavier memory and bandwidth requirements and potentially unstable training.

Taken together, these factors demonstrate that setting $scale = 2$ provides the optimal trade-off between recall and efficiency in datasets dominated by small objects, and we therefore adopt it as the fixed parameter in the SPD module of TinyDef-DETR.

3.3.3. Design of the Subsequent Convolution

Following SPD, we adopt a carefully designed convolutional layer to refine the rearranged features. Specifically, we employ a non-strided convolution with a kernel size of 3×3 . This configuration is chosen because the 3×3 kernel provides the minimal receptive field capable of covering the 2×2 local neighborhood that is redistributed during SPD. In contrast, a 1×1 kernel would only perform channel mixing without explicitly modeling cross-partition spatial relationships, which are essential for capturing subtle structural variations in small defects. Larger kernels such as 5×5 would increase computation without offering proportional benefits for objects of the scale encountered in transmission line inspection.

We set the stride to 1 in order to avoid any additional downsampling. Since the primary motivation of SPD is to preserve pixel-level detail while reducing resolution in a lossless manner, further spatial reduction at this stage would counteract the benefits of SPD and degrade the detection of small defects.

In terms of channel configuration, the input dimensionality after SPD expands to four times the original number of channels, consistent with $\text{scale} = 2$. This expansion ensures that all pixel-level information is preserved in the channel space. The output channel dimension is then set to match the base width of the subsequent stage in TinyDef-DETR, ensuring both computational efficiency and stable gradient propagation across the backbone.

3.4. Cross-Stage Dual-Domain Multi-Scale Attention Module

In transmission line defect detection, most targets are small-scale objects such as cracks, rust spots, or insulator damages. These defects often exhibit weak visual saliency and subtle structural variations, making them difficult to distinguish from complex backgrounds such as vegetation, sky, or towers. Conventional convolutional networks are limited by their local receptive fields, while large kernels may cause oversmoothing and incur high computational costs. Similarly, traditional attention mechanisms focusing solely on spatial or channel domains fail to provide sufficient enhancement for ambiguous and small targets. Therefore, a more effective mechanism is required to preserve fine-grained details, capture global semantics, and adaptively highlight defect-related features.

To address these challenges, we propose the Cross-Stage Dual-Domain Multi-Scale Attention Module (CSDMAM). Given input features $X \in \mathbb{R}^{B \times C \times H \times W}$, we first employ a 1×1 convolution to adjust the channel dimension. The transformed features are then fed into parallel branches: a large-receptive-field branch, a local branch, and a dual-domain Frequency-Spatial-Channel Attention (FSCA) branch. The outputs are aggregated through residual summation and projected by a 1×1 convolution to form the final response. To provide a clearer understanding of the proposed design, the overall architecture of CSDMAM is illustrated in Figure 5.

To effectively capture different types of information, we incorporate four complementary branches into the module.

Specifically, to enlarge the receptive field, we add a large-receptive-field branch employing depth-wise convolutions with kernel sizes (k, k) , $(1, k)$, $(k, 1)$, where $k = 31$. The square kernel models global contextual information, while the strip kernels capture elongated dependencies along horizontal and vertical directions, which are especially important for line-shaped structures in transmission infrastructure.

To preserve fine-grained local cues, we further introduce a local branch with a lightweight depth-wise 1×1 convolution, ensuring that subtle defects such as cracks or corrosion spots are not smoothed out by large-kernel operations.

To strengthen semantic discrimination, we design a Frequency-Spatial-Channel Attention (FSCA) branch that jointly exploits frequency, spatial, and channel dependencies. Given input features $X \in \mathbb{R}^{B \times C \times H \times W}$, we first apply the two-dimensional Fourier transform to obtain the frequency representation

$$X_f = \mathcal{F}(X),$$

where \mathcal{F} denotes the discrete Fourier transform (DFT). Channel-wise weights are then computed via global average pooling followed by a 1×1 convolution, producing $A_c \in \mathbb{R}^{B \times C \times 1}$. The enhanced frequency map is obtained as

$$\tilde{X}_f = A_c \cdot X_f,$$

which is reconstructed into the spatial domain using the inverse DFT:

$$X_{fs} = \mathcal{F}^{-1}(\tilde{X}_f).$$

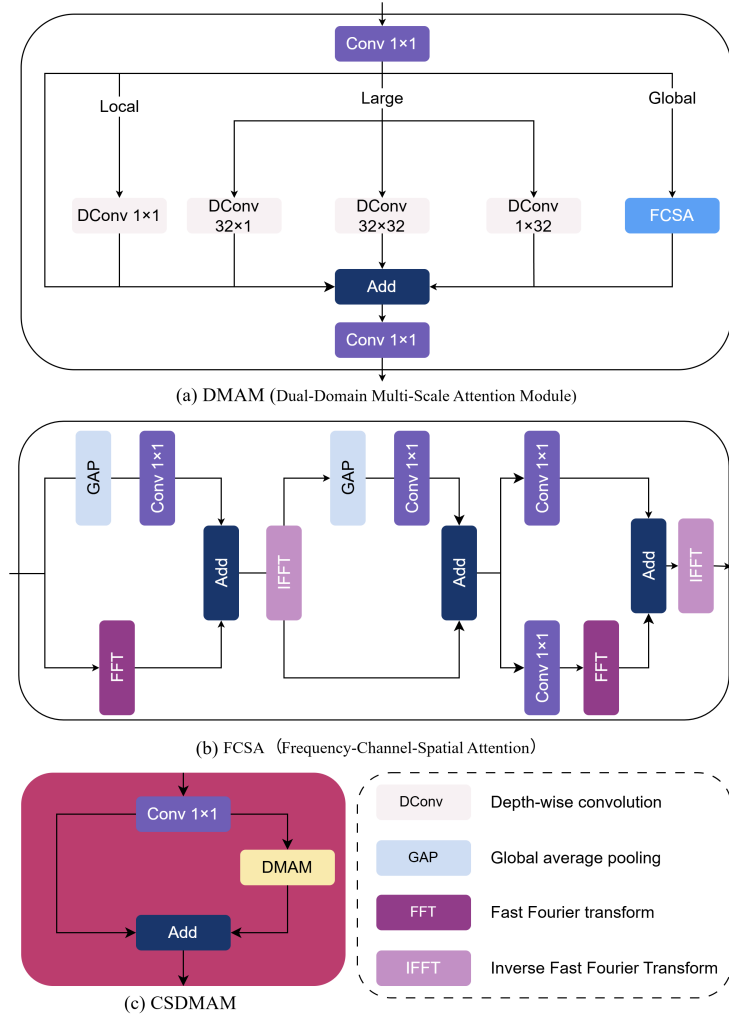


Figure 5. The architecture of Cross-Stage Dual-Domain Multi-Scale Attention Module (CSDMAM).

An additional spatial–channel reweighting map A_{sc} is generated by global pooling and a 1×1 convolution, yielding the FSCA-enhanced representation

$$X_{fscs} = A_{sc} \cdot X_{fs}.$$

The outputs of all branches are fused with the residual input to form the aggregated response:

$$Y = X + DW_{1,k}(X_n) + DW_{k,1}(X_n) + DW_{k,k}(X_n) + DW_{1,1}(X_n) + X_{fscs},$$

where DW denotes depth-wise convolution with the specified kernel size. Finally, to improve efficiency and gradient propagation, we extend the design into a cross-stage structure. Following the Cross Stage Partial (CSP) strategy, the input is divided into two parts: one processed by the multi-branch attention operations and the other preserved as an identity mapping. The two parts are concatenated and fused through a 1×1 convolution, giving the final output

$$Y_{cs} = \text{Conv}([\text{DMAM}(X_{\text{branch}}), X_{\text{identity}}]).$$

By combining large receptive fields, local detail preservation, and FSCA-based dual-domain enhancement within a cross-stage framework, CSDMAM achieves a favorable balance be-

tween global semantic understanding and precise defect localization, making it particularly effective for detecting small, visually ambiguous targets in UAV inspection imagery.

3.5. Focaler-Wise-SIoU Loss Function

In the task of transmission line defect detection, where the majority of objects are small and often exhibit subtle spatial differences, accurate bounding box regression plays a crucial role. IoU-based loss functions have become the de facto standard for this purpose in modern object detectors, yet they still suffer from several inherent limitations. The vanilla IoU loss only considers the overlap ratio and fails to capture spatial misalignment when boxes do not intersect. Its variants, such as GIoU[34], DIoU[35], and CIoU[36], partially alleviate this issue by introducing penalties related to enclosure area, center distance, or aspect ratio. However, these approaches remain limited in their ability to jointly model geometric alignment and shape consistency. More advanced designs such as SIoU[37] attempt to incorporate angular, distance, and shape discrepancies, providing richer geometric information. Nevertheless, they still treat all samples equally, regardless of their difficulty, which results in an imbalanced gradient contribution. Easy samples dominate the optimization, while hard samples, particularly those corresponding to small defects with low signal-to-noise ratios, receive insufficient emphasis. Furthermore, in high-IoU regimes where precise localization is critical for tiny defect regions, conventional losses often lack discriminative power, leading to slower convergence and degraded accuracy.

To address these limitations, we propose the Focaler-Wise-SIoU Loss, which integrates normalized IoU scaling, comprehensive geometric penalties, and a non-monotonic focal modulation scheme. This loss is specifically designed to enhance sensitivity in high-IoU regimes and to dynamically reweight samples according to their difficulty, making it particularly suitable for datasets dominated by small and challenging targets such as transmission line defects.

Formally, given a predicted box $B_p = (x_p, y_p, w_p, h_p)$ and a target box $B_t = (x_t, y_t, w_t, h_t)$, both parameterized by center coordinates and width-height pairs, we first convert them into corner representation (x_1, y_1, x_2, y_2) . The intersection and union regions are then computed, yielding the standard Intersection over Union score:

$$IoU = \frac{S_{int}}{S_{union}}. \quad (5)$$

To improve discriminability in high-IoU ranges, we apply Focal-IoU normalization, which linearly maps IoU into the interval $[0, 1]$ as:

$$IoU = \text{clip}\left(\frac{|IoU - d|}{u - d}, 0, 1\right), \quad (6)$$

where $d = 0$ and $u = 0.95$. The base penalty is then defined as $I_{IoU} = 1 - IoU$.

On top of this formulation, we incorporate the Scylla-IoU (SIoU) penalty, which considers angle, distance, and shape discrepancies. The angular component is derived from the displacement between box centers $\Delta = (d_x, d_y)$ as:

$$\phi = \arcsin\left(\frac{\min(|d_x|, |d_y|)}{\sqrt{d_x^2 + d_y^2 + 10^{-4}}}\right), \quad (7)$$

$$\text{Angle} = \sin(2\phi) - 2. \quad (8)$$

This term modulates the distance penalty:

$$\text{Dist} = 2 - \exp\left(\text{Angle} \cdot \frac{d_x}{w_{box}}\right) - \exp\left(\text{Angle} \cdot \frac{d_y}{h_{box}}\right), \quad (9)$$

where (w_{box}, h_{box}) denote the dimensions of the smallest enclosing box. To model shape consistency, we define the shape cost as:

$$\text{Shape} = \left(1 - \exp\left(-\frac{|w_p - w_t|}{\max(w_p, w_t)}\right)\right) + \left(1 - \exp\left(-\frac{|h_p - h_t|}{\max(h_p, h_t)}\right)\right)^\theta, \quad (10)$$

with $\theta = 4$. The SIoU core-loss is then expressed as:

$$L_{SIoU} = L_{IoU} + \frac{\text{Dist} + \text{Shape}}{2}. \quad (11)$$

To ensure adaptive treatment of samples, particularly the abundance of small and hard defect targets, we introduce a Wise modulation mechanism. A relative difficulty factor is defined as:

$$\beta = \frac{L_{IoU}}{\mathbb{E}[L_{IoU}]}. \quad (12)$$

where $\mathbb{E}[L_{IoU}]$ is an exponential moving average updated with a momentum of 10^{-2} . Unlike conventional monotonic modulations, which continuously emphasize harder cases, we employ a non-monotonic focal modulation (V3) strategy to avoid over-penalization of extreme outliers:

$$\gamma(\beta) = \frac{\beta}{\delta \cdot \alpha^{(\beta-\delta)}}. \quad (13)$$

This modulation adaptively emphasizes moderately difficult samples while suppressing trivial and excessively noisy cases, which is particularly beneficial for stabilizing training in small-object detection.

Finally, the complete Focaler-Wise-SIoU Loss is formulated as:

$$L = \left(1 - I\hat{o}U + \frac{\text{Dist} + \text{Shape}}{2}\right) \cdot \frac{1 - IoU}{\mathbb{E}[1 - IoU]} \cdot \frac{1 - IoU}{\mathbb{E}[1 - IoU]}^\delta. \quad (14)$$

This unified design preserves the interpretability of IoU-based losses while enhancing discriminative power in high-IoU regimes, adaptively balancing sample contributions, and stabilizing optimization. As a result, the Focaler-Wise-SIoU Loss is particularly effective in transmission line defect detection, where most targets are small, difficult to localize, and require precise bounding box regression.

4. Evaluation and results analysis

4.1. CSG-ADCD

The CSG-ADCD (China Southern Grid Aerial Defective Component Dataset) is a large-scale, high-resolution UAV-based image dataset specifically developed for the detection of defects in power transmission line components, including insulators, tie wires, and poles. Constructed under authentic inspection scenarios by China Southern Power Grid, the dataset comprises 10,000 carefully selected aerial images. Each image was manually annotated by a single domain expert to ensure both consistency and high-quality labeling.

In total, the dataset contains 73,448 annotated instances covering nine component states or defect types: Normal Insulator (zcyjz), Polluted Insulator (jyzwh), Damaged Pole (dgss), Missing Tie Wire (zxqs), Loose Tie Wire (zxst), Insulator Flashover (jyzsl), Bird Nest (nw), Broken Insulator (jyzps), and Shattered Post Insulator (zyzsl). Among these, Normal

Insulator is the dominant class with 43,808 instances, whereas Shattered Post Insulator is the rarest with only 37 instances.

Table 1 provides a correspondence between the labels and category names for each defect type in the dataset, offering a clear overview of the classification scheme used.

Table 1. The correspondence between labels and category names.

NO	Label	Name
0	zcjyz	Normal Insulator
1	jyzwh	Polluted Insulator
2	dgss	Damaged Pole
3	zxqs	Missing Tie Wire
4	zxst	Loose Tie Wire
5	jyzsl	Insulator Flashover
6	nw	Bird Nest
7	jyzps	Broken Insulator

On average, each object occupies a pixel area of 422.12, with the dataset exhibiting a highly imbalanced distribution in terms of object sizes: 94.51% small objects (69,413 instances), 5.48% medium-sized (4,022 instances), and only 0.02% large (13 instances). This reflects the intrinsic characteristics of UAV-based transmission line inspection targets, which are often small, localized, and partially occluded.

For training consistency, all images were preprocessed by resizing the longer side to 640 pixels while preserving aspect ratio, followed by padding to a fixed resolution of 640 × 640 pixels using gray borders. The dataset is split into 8,000 training, 1,000 validation, and 1,000 test images.

Statistical analysis further highlights two key features of the dataset. First, the scatter distribution of object width and height reveals a strong concentration of samples in the lower-left region, confirming the overwhelming dominance of small-scale objects. Second, the number of objects per image follows a relatively stable distribution, averaging 7.34 instances per image, with 2,285 images containing between 7 and 8 objects. This regularity is particularly beneficial for developing models optimized for dense and small-object detection.

In summary, the CSG-ADCD dataset demonstrates strong representativeness by simultaneously addressing two critical aspects. On the one hand, it captures a comprehensive range of component defects and status indicators that are directly relevant to transmission safety, while also reflecting the complexity of real-world inspection conditions such as occlusion, cluttered backgrounds, and varying illumination. On the other hand, its pronounced dominance of small-scale objects—over 94% of all annotated instances—together with the presence of subtle and fine-grained anomalies, makes it a highly challenging and domain-specific benchmark. In this regard, CSG-ADCD not only advances research in defect detection for power systems but also provides a valuable testbed for generic small-object detection in aerial remote sensing, offering greater domain relevance than existing datasets such as VisDrone[38].

Overall, CSG-ADCD constitutes a robust and high-fidelity benchmark, offering significant value for advancing research in both domain-specific defect detection and general small-object detection tasks.

As shown in Fig.6, the vast majority of objects are smaller than 32×32 pixels, placing them within the small-object category. The scatter plot depicts the distribution of annotated instances by pixel width and height after preprocessing, with different categories distinguished by distinct colors in the legend. The strong concentration of points in the lower-left corner highlights the predominance of small and compact targets, consistent

with the characteristics of transmission-line inspection imagery. Dashed reference lines at 32×32 and 96×96 pixels mark the boundaries between small, medium, and large regimes, clearly revealing the relative scarcity of medium- and large-sized objects. Overall, the visualization emphasizes the dominance of small instances and underscores the dense, fine-grained nature of aerially captured transmission-line defects.

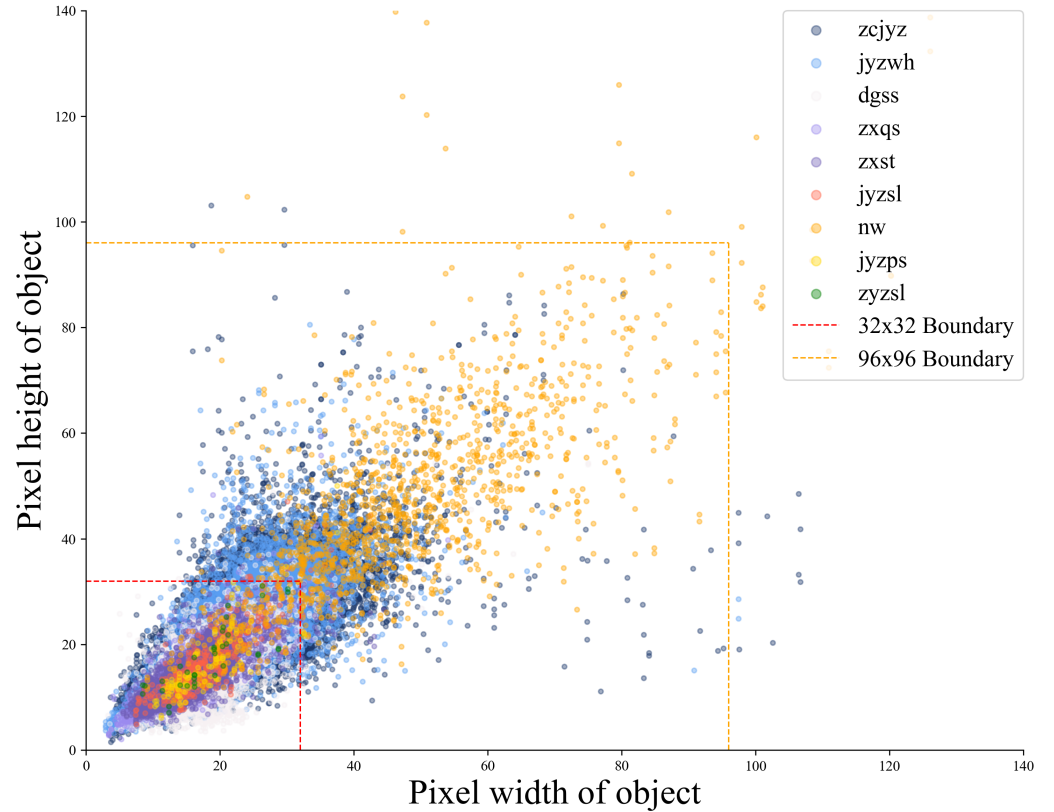


Figure 6. Distribution of object sizes in CSG-ADCD

4.2. Model Training and Evaluation Metrics

The proposed model is implemented based on the PyTorch deep learning framework and is built upon the RE-DETR architecture released by Ultralytics. Training is conducted on a high-performance workstation equipped with NVIDIA GeForce RTX 3090 GPU with 24 GB of memory. The software environment consists of Ubuntu 20.04, Python 3.10.14, PyTorch 2.3.1, and CUDA 12.1, enabling efficient GPU acceleration. The model is trained for 100 epochs using the AdamW optimizer.

In the task of UAV-based power transmission line defect detection, the performance of different detection algorithms may vary significantly under diverse operational scenarios. The inference capability of a detection model is typically evaluated using several criteria, including: the computational complexity measured in floating-point operations (FLOPs), and a series of key performance metrics such as precision (P), recall (R), average precision (AP), and mean average precision (mAP). These metrics are formally defined as follows:

$$P = \frac{TP}{TP + FP}$$

Precision (P) measures the proportion of correctly detected defect instances among all predicted defect instances. A higher precision indicates that the model produces fewer false alarms (false positives), which is critical for avoiding unnecessary inspection or maintenance actions.

$$R = \frac{TP}{TP + FN}$$

Recall (R) reflects the proportion of correctly detected defect instances among all actual defect instances. A higher recall indicates that the model misses fewer true defects (false negatives), which is essential for ensuring the completeness of defect identification in safety-critical applications.

$$AP = \int_0^1 P(R) dR$$

The average precision (AP) is computed as the area under the precision–recall curve. It captures the trade-off between precision and recall across different confidence thresholds, providing a more comprehensive evaluation of the detection performance for a single defect category.

$$mAP = \frac{1}{k} \sum_{i=1}^k AP_i$$

The mean average precision (mAP) represents the mean value of AP over k defect categories. It is widely recognized as the most comprehensive metric for evaluating detection models, as it jointly considers both detection accuracy and robustness across multiple defect types.

In addition to these general measures, the COCO evaluation protocol further defines scale-sensitive metrics, such as: AP_s and AP_m , to provide deeper insights into detection performance across different object sizes. Specifically, AP_s evaluates the average precision for small objects (with areas less than 32^2 pixels), while AP_m measures the average precision for medium-sized objects (with areas between 32^2 and 96^2 pixels). Since the majority of defects in transmission line inspection datasets are small in scale, AP_s serves as a particularly critical indicator, directly reflecting the model's capability to capture subtle and fine-grained defect patterns that occupy only a limited number of pixels. Therefore, the COCO metrics AP_s and AP_m are employed in this study to assess detection performance across different object scales.

Here, TP (true positives) denotes the number of correctly detected defect instances, FP (false positives) refers to non-defect regions mistakenly identified as defects, FN (false negatives) indicates defect regions that were not detected, and k denotes the total number of defect categories. Together, these metrics provide a balanced overall performance in terms of accuracy, completeness, and overall reliability, which is important for real-time transmission line inspection tasks.

4.3. Comparison of heatmaps

To intuitively demonstrate the effectiveness of the proposed modules, we generate heatmaps from the baseline RT-DETR model and the model with the proposed modules (EE-ResNet, SPD Convolution, and CSDMAM) on the same input image. These heatmaps illustrate the attention distribution of the models during the recognition process. As shown in Fig.7, subfigures (a), (c), and (e) represent the attention maps from the baseline model corresponding to the modules before integration, while subfigures (b), (d), and (f) show the attention maps after incorporating the proposed modules. It can be observed that the attention distribution after the inclusion of the modules is more fine-grained, and the target contours are more distinct, indicating that the proposed modules enhance the model's ability to preserve more detailed information.

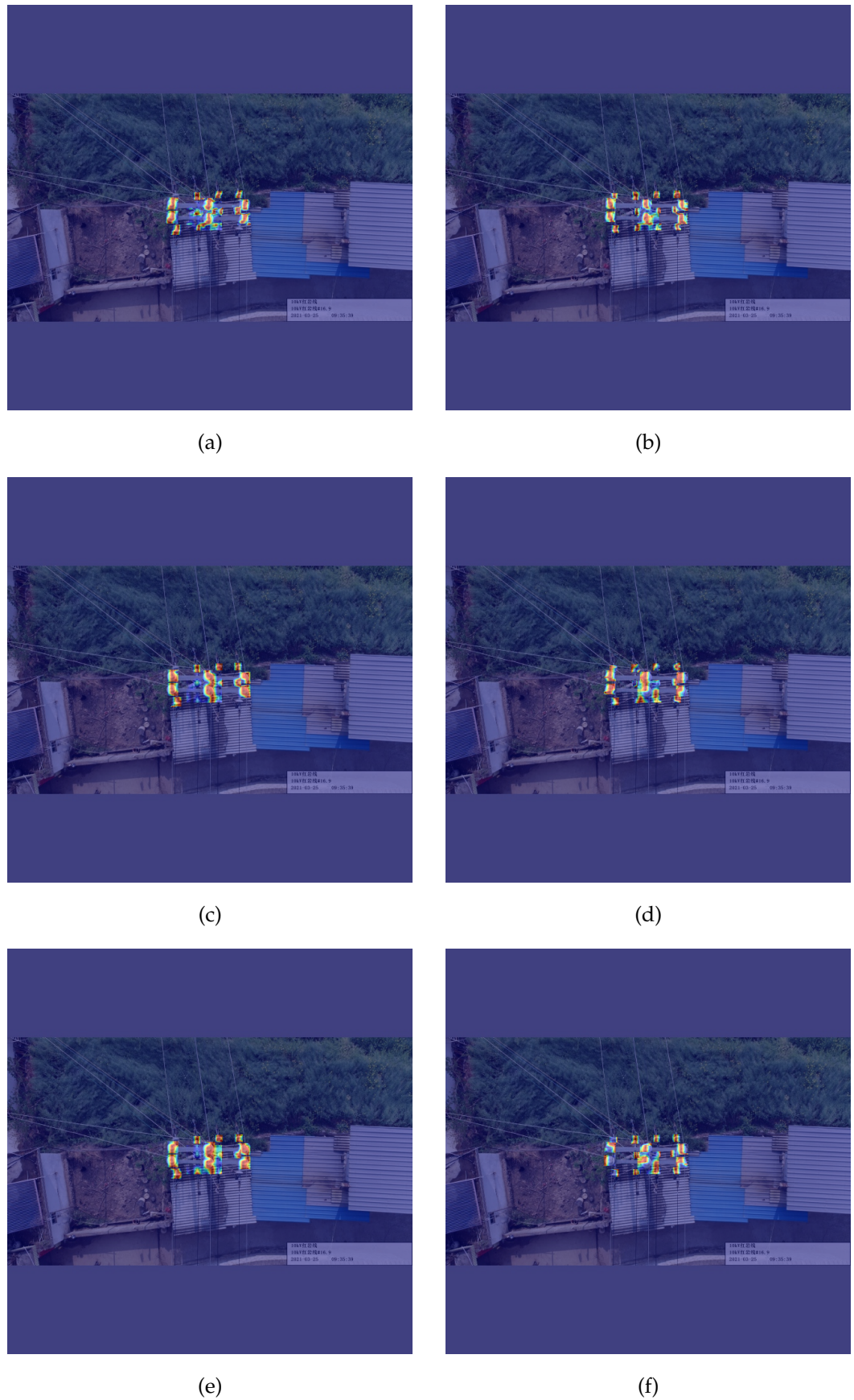


Figure 7. Comparison of attention maps for the baseline RT-DETR model before and after incorporating different innovative modules: (a) without EEBlock, (b) with EEBlock, (c) without SPD Convolution, (d) with SPD Convolution, (e) without CSDMAM, (f) with CSDMAM.

4.4. Ablation Study of the Proposed Method

To analyze the impact of each innovative component in CSG-ADCD, we conducted ablation experiments by systematically including and excluding four key modules: EER (Edge-Enhanced ResNet), SPD (Stride-free Space-to-Depth), CSDMAM (Cross-Stage Dual-Domain Multi-Scale Attention Module), and FWS Loss (Focaler-Wise-SIoU Loss). The results, shown in Table 2, demonstrate the contribution of each module to the model's overall performance across various evaluation metrics.

Table 2. Ablation Experiments for CSG-ADCD

EER	SPD	CSDMAM	FWSLoss	GFLOPs	Precision	Recall	mAP ₅₀	AP _s
×	×	×	×	57.0	0.369	0.177	0.163	0.071
✓	×	×	×	57.0	0.444	0.203	0.189	0.073
✓	✓	×	×	59.9	0.486	0.195	0.190	0.083
✓	×	✓	×	72.8	0.458	0.166	0.165	0.072
✓	×	×	✓	57.0	0.500	0.204	0.207	0.082
✓	✓	×	×	59.7	0.417	0.208	0.192	0.076
✓	×	✓	×	66.0	0.425	0.190	0.189	0.077
✓	✓	✓	×	65.2	0.385	0.192	0.182	0.072
✓	✓	✓	×	65.3	0.485	0.233	0.237	0.119
✓	✓	✓	✓	65.3	0.534	0.263	0.275	0.106

Edge Enhanced ResNet (EER) As shown in the table, enabling Edge Enhanced ResNet significantly improves the model's precision and recall. Precision increases from 0.369 to 0.444, while recall increases from 0.177 to 0.203. This suggests that Edge Enhanced ResNet effectively refines error estimation, leading to better model accuracy, particularly in complex scenarios. Additionally, mAP₅₀ improves from 0.163 to 0.189, further reflecting the positive impact of this module on object detection. Given that transmission line defect detection typically involves small, often faint features in images, EER plays a crucial role in enhancing the model's sensitivity to these subtle defects.

Space-to-depth Convolution (SPD) Incorporating Space-to-depth Convolution leads to further performance improvements. Precision increases from 0.444 to 0.486, while recall remains relatively consistent at 0.195. The mAP₅₀ also improves from 0.189 to 0.190, which shows that Space-to-depth Convolution is effective in fine-tuning object localization and enhancing precision without a significant trade-off in recall. Given the small scale of defects in transmission line imagery, SPD effectively helps capture more fine-grained spatial information, which improves the localization of small defects in the images.

Cross-Stage Dual-Domain Multi-Scale Attention Module (CSDMAM) Adding the Cross-Stage Dual-Domain Multi-Scale Attention Module results in a slight decrease in performance. Specifically, precision drops from 0.486 to 0.458, and recall decreases from 0.195 to 0.166. The mAP₅₀ metric also drops from 0.190 to 0.165, indicating that although this module may help suppress complex background interference, it slightly compromises the model's accuracy in this configuration. Given that transmission line defects are typically small and can be visually close to background features, this module's background suppression may sometimes inadvertently impact the model's ability to detect small-scale defects.

Focaler-Wise-SIoU Loss (FWS Loss) The inclusion of Focaler-Wise-SIoU Loss leads to significant improvements across all metrics. Precision increases from 0.458 to 0.500, and recall increases from 0.166 to 0.204. mAP₅₀ improves from 0.165 to 0.207, confirming that this loss function enhances model robustness, especially in challenging detection tasks. The AP_s also shows a marked improvement, increasing from 0.071 to 0.119. This improvement is especially important for the transmission line defect detection task, where small defects

make up the majority of the dataset. The FWS Loss function is particularly effective in boosting the model’s sensitivity to small object detection without compromising overall performance.

4.5. Comparisons With Previous Methods

In this section, we conduct a rigorous comparative study between the proposed TinyDef-DETR and representative state-of-the-art detectors spanning one-stage (e.g., YOLOv5/8/10/11), two-stage/cascade paradigms, and Transformer-based frameworks (e.g., RT-DETR, Conditional-DETR, DINO). All models are evaluated under a unified protocol—identical data splits, input resolution, and training hyperparameters—to ensure fairness.

Before presenting the experimental data, to visually highlight the differences between TinyDef-DETR and other representative detectors, we conduct a case study on four representative images from the CSG-ADCD dataset. To save space and facilitate readability in a scenario where the majority of targets are small objects, we render the detection bounding boxes with filled colors rather than outlines only. This visualization provides a clearer comparison of recognition results across different models, and the detection results are illustrated in Fig. 8.

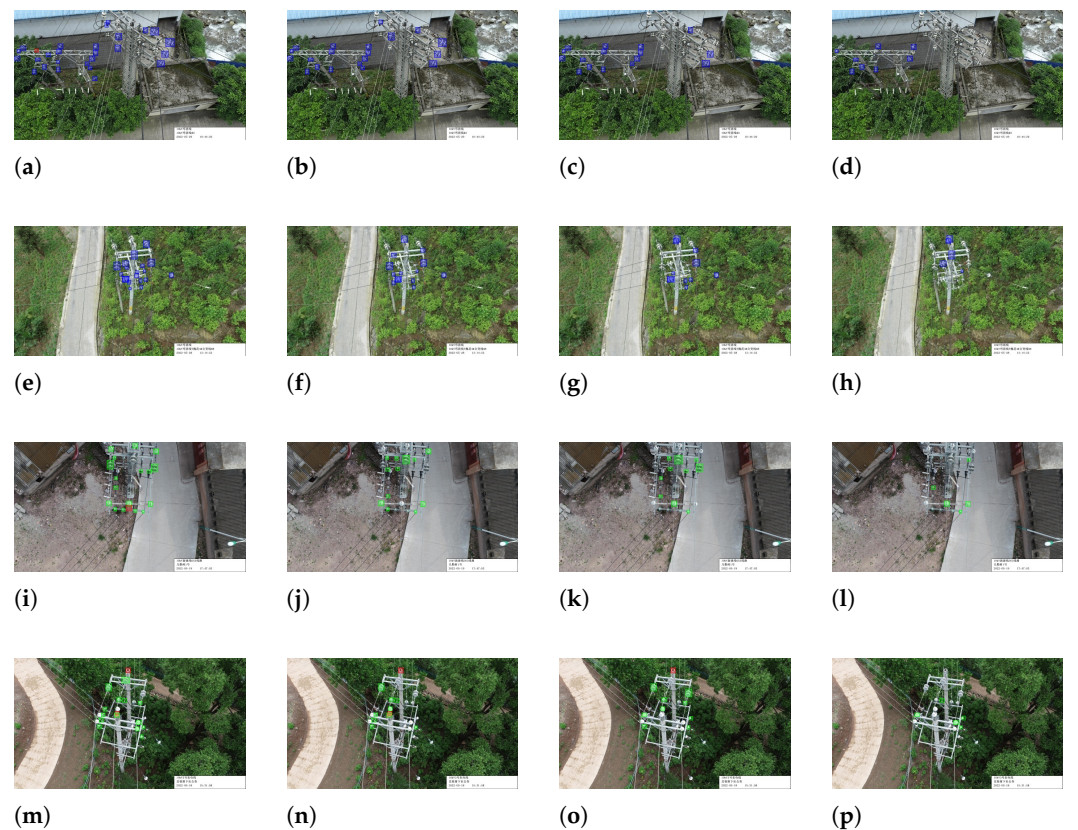


Figure 8. Comparison of detection results from four object detection methods on four representative test samples. Rows (a)–(d) correspond to different test images, and the four columns show the results obtained by TinyDef-DETR, DINO, RT-DETR-R18, and YOLO v5s, respectively.

Table 3 summarizes the overall performance of representative detectors on the CSG-ADCD dataset. The comparison covers lightweight and standard variants of YOLO (v5, v8, v10, v11), Transformer-based models such as RT-DETR and Conditional-DETR, as well as classical baselines including RetinaNet and DETR. Key indicators, including the number of parameters, computational complexity (GFLOPs), Precision, Recall, mAP_{50} , and $mAP_{50:95}$,

are reported to provide a comprehensive view of accuracy–efficiency trade-offs. The best values in each column are highlighted in bold for clarity.

In addition, part of the models are implemented with MMDetection, an open-source object detection toolbox based on PyTorch, which is a core component of the OpenMMLab[39] project. This ensures standardized training pipelines, reproducibility, and fair comparison across different architectures.

It is also worth noting that although DINO achieves slightly higher performance than TinyDef-DETR on certain metrics, its training requires approximately 79.8 hours, which is significantly longer. Such excessive training time limits its practical applicability in real-world UAV-based inspection tasks, whereas TinyDef-DETR achieves a more balanced trade-off between accuracy and efficiency.

Table 3. Model Performance Evaluation: Precision, Recall, and mAP for CSG-ADCD (best results highlighted in bold).

Model	Parameters (M)	GFLOPs	Precision	Recall	mAP ₅₀	mAP _{50:95}
YOLO v5n	2.2	5.8	0.707	0.131	0.131	0.0628
YOLO v5s	9.1	23.8	0.346	0.148	0.140	0.0646
YOLO v5m	25.1	64.0	0.548	0.164	0.162	0.0717
YOLO v8n	2.7	6.8	0.580	0.134	0.133	0.0613
YOLO v8s	11.1	28.5	0.375	0.155	0.147	0.0661
YOLO v8m	23.2	67.5	0.403	0.169	0.163	0.0719
YOLO 10n[40]	2.7	8.2	0.707	0.125	0.133	0.0627
YOLO 10s	8.0	24.5	0.536	0.144	0.157	0.0725
YOLO 10m	16.6	63.5	0.386	0.170	0.162	0.0753
YOLO 11n[41]	2.6	6.3	0.638	0.135	0.136	0.0641
YOLO 11s	9.4	21.3	0.516	0.166	0.155	0.0717
YOLO 11m	20.0	67.7	0.399	0.181	0.173	0.0776
RT-DETR-l	32.8	108.0	0.480	0.189	0.199	0.0890
RT-DETR-x	65.5	222.5	0.485	0.199	0.216	0.0990
RT-DETR-R18	19.8	57.0	0.369	0.177	0.163	0.0738
RT-DETR-R34	31.2	88.8	0.354	0.127	0.117	0.0533
RT-DETR-R50	42.9	134.8	0.363	0.120	0.115	0.0514
RT-DETR-R101	74.7	247.1	0.467	0.185	0.193	0.0879
Conditional-DETR-R18[42]	–	–	0.309	0.068	0.038	0.0110
Conditional-DETR-R34	–	–	0.447	0.082	0.034	0.0090
Conditional-DETR-R50	44.0	89.5	0.568	0.159	0.172	0.0660
DETR-R50[43]	–	–	0.301	0.138	0.124	0.0430
RetinaNet[44]	12.0	33.8	0.394	0.029	0.013	0.0040
DINO[45]	–	–	0.496	0.257	0.224	0.0986
FFCA-YOLO[46]	7.1	51.4	0.680	0.130	0.142	0.0596
TinyDef-DETR	20.5	65.3	0.534	0.263	0.275	0.1187

To further highlight performance on small objects and defect-specific categories, Table 4 reports additional evaluation metrics. These include Recall and mAP₅₀ for Polluted Insulator (jyzwh) and Damaged Pole (dgss), alongside scale-sensitive measures AP_s and AP_m. Such results enable a fine-grained comparison of detection capabilities under challenging UAV inspection scenarios.

Table 4. Model Performance Metrics: Recall, mAP₅₀, AP_s, and AP_m for jyzwh and dgss

Model	Recall (jyzwh)	mAP ₅₀ (jyzwh)	mAP ₅₀ (dgss)	AP _s	AP _m
YOLO v5n	0.352	0.315	0.258	0.061	0.097
YOLO v5s	0.377	0.314	0.270	0.065	0.098
YOLO v5m	0.372	0.367	0.277	0.079	0.081
YOLO v8n	0.364	0.321	0.264	0.066	0.078
YOLO v8s	0.388	0.331	0.269	0.067	0.095
YOLO v8m	0.378	0.360	0.296	0.075	0.087
YOLO 10n[40]	0.352	0.321	0.251	0.062	0.094
YOLO 10s	0.343	0.341	0.308	0.078	0.095
YOLO 10m	0.390	0.356	0.294	0.075	0.097
YOLO 11n[41]	0.353	0.324	0.245	0.060	0.103
YOLO 11s	0.381	0.344	0.291	0.074	0.100
YOLO 11m	0.382	0.373	0.307	0.082	0.094
RT-DETR-l	0.360	0.341	0.372	0.078	0.044
RT-DETR-x	0.366	0.363	0.403	0.083	0.058
RT-DETR-R18	0.347	0.316	0.354	0.071	0.039
RT-DETR-R34	0.293	0.260	0.284	0.056	0.062
RT-DETR-R50	0.278	0.254	0.275	0.054	0.027
RT-DETR-R101	0.345	0.316	0.378	0.073	0.050
Conditional-DETR-R18[47]	0.150	0.073	0.082	0.009	0.016
Conditional-DETR-R34	0.184	0.063	0.059	0.006	0.011
Conditional-DETR-R50	0.406	0.389	0.287	0.064	0.057
DETR-R50[43]	0.289	0.280	0.203	0.041	0.037
RetinaNet[44]	0.048	0.022	0.006	0.012	0.003
DINO[45]	0.437	0.420	0.426	0.085	0.075
FFCA-YOLO[46]	0.286	0.291	0.270	0.059	0.051
TinyDef-DETR	0.397	0.391	0.419	0.106	0.110

To further illustrate the trade-off between detection accuracy and computational efficiency, the results reported in Table 3 are visualized in Fig. 9. The plot highlights the relative positions of different detectors in terms of mAP₅₀ versus GFLOPs, enabling an intuitive comparison of accuracy–efficiency balance across lightweight YOLO variants, Transformer-based detectors, and the proposed TinyDef-DETR. Notably, TinyDef-DETR achieves an mAP₅₀ of 0.275 with a computational cost of only 65.3 GFLOPs, striking a favorable balance between accuracy and efficiency compared with both lightweight YOLO models and heavier Transformer-based detectors.

To provide a holistic comparison of different detectors, we visualize their performance across multiple evaluation metrics in the form of a radar chart (Fig. 10). The selected models include YOLOv5s, YOLOv8s, YOLO11s, RT-DETR-R18, FFCA-YOLO, and TinyDef-DETR, representing both one-stage and Transformer-based detection paradigms. The evaluation encompasses a comprehensive set of indicators, namely Recall, mAP₅₀, mAP_{50:95}, AP_s, AP_m, Recall of Polluted Insulator (jyzwh), mAP₅₀ of Polluted Insulator, and mAP₅₀ of Damaged Pole (dgss). For enhanced visual comparability, each metric is normalized to its maximum value.

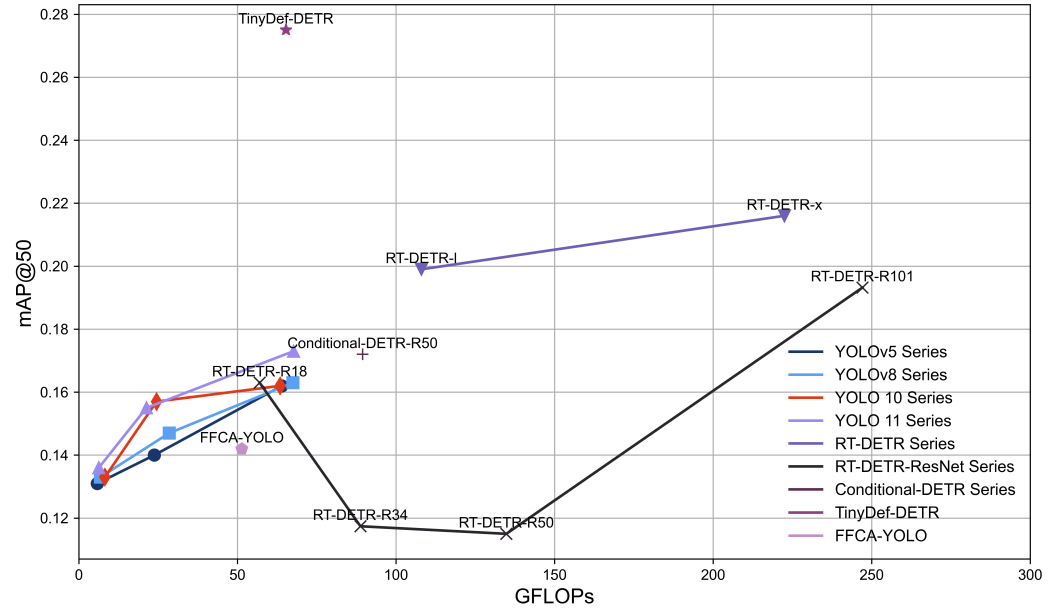


Figure 9. Comparison of model performance in terms of mAP_{50} versus GFLOPs. For clarity and to save space, labels for YOLO series are omitted; within each series, the models are ordered by GFLOPs from left to right as n, s, and m.

4.6. Generalization Experiments for the Proposed Methods

Since small objects account for a large proportion in this dataset, to further validate the generalization capability of the proposed method, we additionally conduct generalization experiments on the VisDrone[38] dataset. VisDrone is a large-scale benchmark dataset specifically constructed for visual perception tasks under the perspective of unmanned aerial vehicles (UAVs). Created by the Aerial Vision Group at the University of Science and Technology of China, the dataset comprises over 26,000 high-resolution images and 263 video sequences, captured across diverse urban and suburban environments such as streets, rooftops, playgrounds, and traffic scenes. It includes more than 100,000 manually annotated object instances spanning 10 common categories, including pedestrians, cars, buses, trucks, bicycles, and others. Each object is labeled with rich metadata, including bounding boxes, object class, occlusion level, and truncation ratio. Due to its dense object distribution, high proportion of small objects, severe occlusion, and large-scale variation in viewpoint and illumination, VisDrone presents considerable challenges for detection and tracking models. Consequently, it has been widely adopted as a standard benchmark to evaluate the robustness and generalization ability of UAV-based visual recognition algorithms in real-world complex scenarios. To further assess the generalization capability of the proposed TinyDef-DETR, we conducted experiments on the VisDrone dataset and compared its performance against representative state-of-the-art YOLO series models, FFCA-YOLO, and its baseline RT-DETR-R18. The results are summarized in Table 5, where the best values in each column have been highlighted in bold for clarity.

Table 5. Comparison Experiments for TinyDef-DETR in VisDrone

Model	Param(M)	GFLOPs	mAP_{50}	$mAP_{50:95}$	AP_s	AP_m
YOLOv8n	3.0	8.1	0.259	0.144	0.059	0.225
YOLOv8s	11.1	28.5	0.307	0.173	0.078	0.269
YOLOv8m	25.9	78.7	0.332	0.190	0.090	0.294
YOLO10n[40]	2.3	6.5	0.261	0.142	0.063	0.224

Model	Param(M)	GFLOPs	mAP ₅₀	mAP _{50:95}	AP _s	AP _m
YOLO10s	7.2	21.4	0.323	0.179	0.086	0.278
YOLO10m	15.3	58.9	0.345	0.195	0.097	0.300
YOLO11n[41]	2.6	6.3	0.258	0.142	0.058	0.225
YOLO11s	9.4	21.3	0.313	0.176	0.080	0.272
YOLO11m	20.0	67.7	0.350	0.203	0.098	0.312
YOLO12n[48]	2.6	6.3	0.259	0.142	0.057	0.224
YOLO12s	9.2	21.2	0.312	0.176	0.081	0.274
YOLO12m	20.1	67.2	0.336	0.192	0.094	0.298
YOLO13n[49]	2.5	6.2	0.244	0.133	0.055	0.210
YOLO13s	9.0	20.1	0.297	0.167	0.077	0.258
YOLOX-Tiny[50]	5.0	7.6	0.278	0.148	0.076	0.221
RT-DETR-R18	20.0	60.0	0.333	0.185	0.139	0.275
ATSS-R50[51]	38.9	110.0	0.338	0.204	0.100	0.317
Cascade-RCNN-R50[52]	69.3	236.0	0.326	0.197	0.099	0.309
D-Fine-N[53]	3.7	7.1	0.334	0.183	0.093	0.270
Faster-RCNN-R50[54]	41.4	208.0	0.329	0.194	0.095	0.309
FBRT-YOLO-M[55]	7.4	58.7	0.344	0.196	0.094	0.309
FBRT-YOLO-N	0.8	6.7	0.265	0.148	0.062	0.234
FBRT-YOLO-S	2.9	22.9	0.323	0.183	0.085	0.283
FFCA-YOLO[46]	7.1	51.4	0.267	0.122	0.091	0.295
RetinaNet-R50[44]	36.5	210.0	0.276	0.164	0.060	0.274
RTMDet-Tiny[56]	4.9	8.0	0.312	0.184	0.077	0.288
TOOD-R50[57]	32.0	199.0	0.339	0.204	0.102	0.317
TinyDef-DETR	20.5	65.0	0.372	0.217	0.148	0.348

5. Conclusions

In this paper, we proposed TinyDef-DETR, a DETR-based framework tailored for defect detection in UAV imagery of transmission lines. By integrating an edge-enhanced ResNet backbone, a stride-free space-to-depth module, a cross-stage dual-domain multi-scale attention mechanism, and a Focaler-Wise-SIoU regression loss, the model effectively addresses the challenges posed by small, ambiguous, and background-cluttered defects.

Extensive experiments on the CSG-ADCD dataset, as well as real-world UAV imagery, demonstrated that TinyDef-DETR consistently outperforms representative detectors in terms of detection accuracy, recall, and robustness, while maintaining computational efficiency. Ablation studies further verified the effectiveness of each proposed component, highlighting their complementary contributions to the overall performance.

The results confirm that TinyDef-DETR not only achieves strong detection capability for small and difficult targets but also provides a practical and efficient solution for real-world UAV-based inspection scenarios. Given its modular and lightweight design, the proposed framework holds promise for broader applications in power system inspection and can be extended to other small-object detection tasks in aerial remote sensing.

Author Contributions: For research articles with several authors, a short paragraph specifying their individual contributions must be provided. The following statements should be used “Conceptualization, X.X. and Y.Y.; methodology, X.X.; software, X.X.; validation, X.X., Y.Y. and Z.Z.; formal analysis, X.X.; investigation, X.X.; resources, X.X.; data curation, X.X.; writing—original draft preparation, X.X.; writing—review and editing, X.X.; visualization, X.X.; supervision, X.X.; project administration, X.X.; funding acquisition, Y.Y. All authors have read and agreed to the published version of the

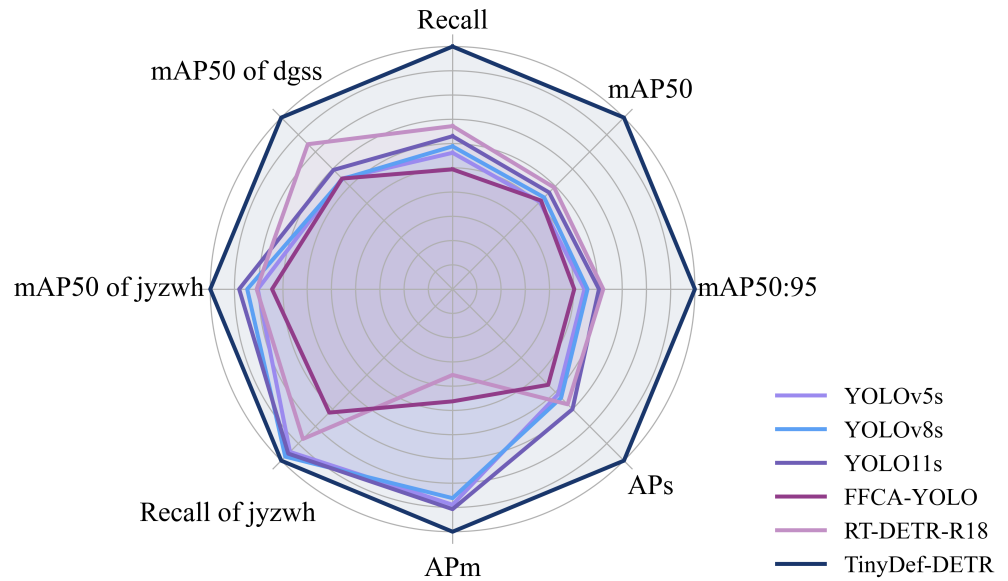


Figure 10. Radar Chart of Performance Comparison on Transmission Line Defect Detection

manuscript.”, please turn to the [CRediT taxonomy](#) for the term explanation. Authorship must be limited to those who have contributed substantially to the work reported.

Funding: Please add: “This research received no external funding” or “This research was funded by NAME OF FUNDER grant number XXX.” and “The APC was funded by XXX”. Check carefully that the details given are accurate and use the standard spelling of funding agency names at <https://search.crossref.org/funding>, any errors may affect your future funding.

Institutional Review Board Statement: In this section, you should add the Institutional Review Board Statement and approval number, if relevant to your study. You might choose to exclude this statement if the study did not require ethical approval. Please note that the Editorial Office might ask you for further information. Please add “The study was conducted in accordance with the Declaration of Helsinki, and approved by the Institutional Review Board (or Ethics Committee) of NAME OF INSTITUTE (protocol code XXX and date of approval).” for studies involving humans. OR “The animal study protocol was approved by the Institutional Review Board (or Ethics Committee) of NAME OF INSTITUTE (protocol code XXX and date of approval).” for studies involving animals. OR “Ethical review and approval were waived for this study due to REASON (please provide a detailed justification).” OR “Not applicable” for studies not involving humans or animals.

Informed Consent Statement: Any research article describing a study involving humans should contain this statement. Please add “Informed consent was obtained from all subjects involved in the study.” OR “Patient consent was waived due to REASON (please provide a detailed justification).” OR “Not applicable” for studies not involving humans. You might also choose to exclude this statement if the study did not involve humans.

Written informed consent for publication must be obtained from participating patients who can be identified (including by the patients themselves). Please state “Written informed consent has been obtained from the patient(s) to publish this paper” if applicable.

Data Availability Statement: Due to the confidentiality of the dataset for this study, participants in this study did not agree to share their data publicly, and therefore supporting data could not be provided.

Acknowledgments: In this section you can acknowledge any support given which is not covered by the author contribution or funding sections. This may include administrative and technical support, or donations in kind (e.g., materials used for experiments). Where GenAI has been used for

purposes such as generating text, data, or graphics, or for study design, data collection, analysis, or interpretation of data, please add “During the preparation of this manuscript/study, the author(s) used [tool name, version information] for the purposes of [description of use]. The authors have reviewed and edited the output and take full responsibility for the content of this publication.”

Conflicts of Interest: The authors declare no conflicts of interest.

References

1. Yang, L.; Fan, J.; Liu, Y.; Li, E.; Peng, J.; Liang, Z. A Review on State-of-the-Art Power Line Inspection Techniques. *IEEE Transactions on Instrumentation and Measurement* **2020**, *69*, 9350–9365.
2. Liu, X.; Miao, X.; Jiang, H.; Chen, J. Data Analysis in Visual Power Line Inspection: An in-Depth Review of Deep Learning for Component Detection and Fault Diagnosis. *Annual Reviews in Control* **2020**, *50*, 253–277.
3. Cheng, Y.; Liu, D. AdIn-DETR: Adapting Detection Transformer for End-to-End Real-Time Power Line Insulator Defect Detection. *IEEE Trans. Instrum. Meas.* **2024**, *73*, 1–11.
4. Yang, Y.; Wang, X. Recognition of Bird Nests on Transmission Lines Based on YOLOv5 and DETR Using Small Samples. *Energy Reports* **2023**, *9*, 6219–6226.
5. Mohsan, S.A.H.; Khan, M.A.; Noor, F.; Ullah, I.; Alsharif, M.H. Towards the Unmanned Aerial Vehicles (UAVs): A Comprehensive Review. *Drones* **2022**, *6*, 147.
6. Ahmed, F.; Mohanta, J.C.; Keshari, A. Power Transmission Line Inspections: Methods, Challenges, Current Status and Usage of Unmanned Aerial Systems. *J Intell Robot Syst* **2024**, *110*, 54.
7. Mirzaei, B.; Nezamabadi-pour, H.; Raouf, A.; Derakhshani, R. Small Object Detection and Tracking: A Comprehensive Review. *Sensors* **2023**, *23*, 6887.
8. Deng, X.; He, M.; Zheng, J.; Qin, L.; Liu, K. Research Progress on Power Visual Detection of Overhead Line Bolt Defects Based on UAV Images. *Drones* **2024**, *8*, 442.
9. Li, Y.; Liu, M.; Li, Z.; Jiang, X. CSSAdet: Real-Time End-to-End Small Object Detection for Power Transmission Line Inspection. *IEEE Trans. Power Delivery* **2023**, *38*, 4432–4442.
10. Redmon, J.; Divvala, S.; Girshick, R.; Farhadi, A. You Only Look Once: Unified, Real-Time Object Detection. In Proceedings of the 2016 IEEE Conference on Computer Vision and Pattern Recognition (CVPR), Las Vegas, NV, USA, 2016; pp. 779–788.
11. Vaswani, A.; Shazeer, N.; Parmar, N.; Uszkoreit, J.; Jones, L.; Gomez, A.N.; ukasz Kaiser, L.; Polosukhin, I. Attention Is All You Need. In Proceedings of the Advances in Neural Information Processing Systems. Curran Associates, Inc., 2017, Vol. 30.
12. Zhao, Y.; Lv, W.; Xu, S.; Wei, J.; Wang, G.; Dang, Q.; Liu, Y.; Chen, J. DETRs Beat YOLOs on Real-time Object Detection. In Proceedings of the 2024 IEEE/CVF Conference on Computer Vision and Pattern Recognition (CVPR), Seattle, WA, USA, 2024; pp. 16965–16974.
13. Lin, T.Y.; Maire, M.; Belongie, S.; Hays, J.; Perona, P.; Ramanan, D.; Dollár, P.; Zitnick, C.L. Microsoft COCO: Common Objects in Context. In *Computer Vision – ECCV 2014*; Fleet, D.; Pajdla, T.; Schiele, B.; Tuytelaars, T., Eds.; Springer International Publishing: Cham, 2014; Vol. 8693, pp. 740–755.
14. Liu, Y.; Liu, D.; Huang, X.; Li, C. Insulator Defect Detection with Deep Learning: A Survey. *IET Generation Trans & Dist* **2023**, *17*, 3541–3558.
15. Deng, X.; He, M.; Zheng, J.; Qin, L.; Liu, K. Research Progress on Power Visual Detection of Overhead Line Bolt Defects Based on UAV Images. *Drones* **2024**, *8*, 442.
16. Yang, L.; Kong, S.; Deng, J.; Li, H.; Liu, Y. DRA-Net: A Dual-Branch Residual Attention Network for Pixelwise Power Line Detection. *IEEE Trans. Instrum. Meas.* **2023**, *72*, 1–13.
17. Liu, X.; Miao, X.; Jiang, H.; Chen, J. Box-Point Detector: A Diagnosis Method for Insulator Faults in Power Lines Using Aerial Images and Convolutional Neural Networks. *IEEE Trans. Power Delivery* **2021**, *36*, 3765–3773.
18. Yu, Z.; Lei, Y.; Shen, F.; Zhou, S.; Yuan, Y. Research on Identification and Detection of Transmission Line Insulator Defects Based on a Lightweight YOLOv5 Network. *Remote Sensing* **2023**, *15*, 4552.
19. Zhang, X.; Zhang, Y.; Shen, K.; Fu, Q.; Shen, H. FAFNet: An Overhead Transmission Line Component Detection Method Based on Feature Alignment and Fusion. *IEEE Sensors J.* **2025**, *25*, 30197–30206.
20. Zhang, X.; Zhang, Y.; Liu, J.; Zhang, C.; Xue, X.; Zhang, H.; Zhang, W. InsuDet: A Fault Detection Method for Insulators of Overhead Transmission Lines Using Convolutional Neural Networks. *IEEE Trans. Instrum. Meas.* **2021**, *70*, 1–12.
21. Tunio, N.A.; Hashmani, A.A.; Khokhar, S.; Tunio, M.A.; Faheem, M. Fault Detection and Classification in Overhead Transmission Lines through Comprehensive Feature Extraction Using Temporal Convolution Neural Network. *Engineering Reports* **2024**, *6*, e12950.
22. Tian, Y.; Ahmad, R.B.; Abdullah, N.A.B. Accurate and Efficient Insulator Maintenance: A DETR Algorithm for Drone Imagery. *PLoS ONE* **2025**, *20*, e0318225.

23. Cheng, Y.; Liu, D. An Image-Based Deep Learning Approach with Improved DETR for Power Line Insulator Defect Detection. *Journal of Sensors* **2022**, *2022*, 1–22.
24. Wang, X.; Yang, T.; Zou, Y. Enhancing Grid Reliability through Advanced Insulator Defect Identification. *PLoS ONE* **2024**, *19*, e0307684.
25. Xie, Z.; Dong, C.; Zhang, K.; Wang, J.; Xiao, Y.; Guo, X.; Zhao, Z.; Shi, C.; Zhao, W. Power-DETR: End-to-end Power Line Defect Components Detection Based on Contrastive Denoising and Hybrid Label Assignment. *IET Generation Trans & Dist* **2024**, *18*, 3264–3277.
26. He, K.; Zhang, X.; Ren, S.; Sun, J. Deep Residual Learning for Image Recognition. In Proceedings of the 2016 IEEE Conference on Computer Vision and Pattern Recognition (CVPR), Las Vegas, NV, USA, 2016; pp. 770–778.
27. Vijayakumar, A.; Vairavasundaram, S. YOLO-based Object Detection Models: A Review and Its Applications. *Multimed Tools Appl* **2024**, *83*, 83535–83574.
28. Ismail, M.S.; Samad, R.; Pebrianti, D.; Mustafa, M.; Hasma Abdullah, N.R. Comparative Analysis of Deep Learning Models for Sheep Detection in Aerial Imagery. In Proceedings of the 2024 9th International Conference on Mechatronics Engineering (ICOM), Kuala Lumpur, Malaysia, 2024; pp. 234–239.
29. Redmon, J.; Farhadi, A. YOLOv3: An Incremental Improvement, 2018, [[arXiv:cs/1804.02767](https://arxiv.org/abs/1804.02767)].
30. Wang, C.Y.; Bochkovskiy, A.; Liao, H.Y.M. YOLOv7: Trainable Bag-of-Freebies Sets New State-of-the-Art for Real-Time Object Detectors. In Proceedings of the 2023 IEEE/CVF Conference on Computer Vision and Pattern Recognition (CVPR), Vancouver, BC, Canada, 2023; pp. 7464–7475.
31. Khanam, R.; Hussain, M. YOLOv11: An Overview of the Key Architectural Enhancements, 2024, [[arXiv:cs/2410.17725](https://arxiv.org/abs/2410.17725)].
32. Wang, Y.; Liu, J.; Zhao, J.; Li, Z.; Yan, Y.; Yan, X.; Xu, F.; Li, F. LCSC-UAVNet: A High-Precision and Lightweight Model for Small-Object Identification and Detection in Maritime UAV Perspective. *Drones* **2025**, *9*, 100.
33. Sunkara, R.; Luo, T. No More Strided Convolutions or Pooling: A New CNN Building Block for Low-Resolution Images and Small Objects. In Proceedings of the Machine Learning and Knowledge Discovery in Databases; Amini, M.R.; Canu, S.; Fischer, A.; Guns, T.; Kralj Novak, P.; Tsoumakas, G., Eds., Cham, 2023; pp. 443–459.
34. Rezatofighi, H.; Tsoi, N.; Gwak, J.; Sadeghian, A.; Reid, I.; Savarese, S. Generalized Intersection Over Union: A Metric and a Loss for Bounding Box Regression. In Proceedings of the 2019 IEEE/CVF Conference on Computer Vision and Pattern Recognition (CVPR), Long Beach, CA, USA, 2019; pp. 658–666.
35. Zheng, Z.; Wang, P.; Liu, W.; Li, J.; Ye, R.; Ren, D. Distance-IoU Loss: Faster and Better Learning for Bounding Box Regression. *Proceedings of the AAAI Conference on Artificial Intelligence* **2020**, *34*, 12993–13000.
36. Zheng, Z.; Wang, P.; Ren, D.; Liu, W.; Ye, R.; Hu, Q.; Zuo, W. Enhancing Geometric Factors in Model Learning and Inference for Object Detection and Instance Segmentation. *IEEE Transactions on Cybernetics* **2022**, *52*, 8574–8586.
37. Gevorgyan, Z. SIoU Loss: More Powerful Learning for Bounding Box Regression, 2022, [[arXiv:cs/2205.12740](https://arxiv.org/abs/2205.12740)].
38. Zhu, P.; Wen, L.; Du, D.; Bian, X.; Fan, H.; Hu, Q.; Ling, H. Detection and Tracking Meet Drones Challenge. *IEEE Transactions on Pattern Analysis and Machine Intelligence* **2022**, *44*, 7380–7399.
39. Chen, K.; Wang, J.; Pang, J.; Cao, Y.; Xiong, Y.; Li, X.; Sun, S.; Feng, W.; Liu, Z.; Xu, J.; et al. MMDetection: Open MMLab Detection Toolbox and Benchmark, 2019, [[arXiv:cs/1906.07155](https://arxiv.org/abs/1906.07155)].
40. Wang, A.; Chen, H.; Liu, L.; Chen, K.; Lin, Z.; Han, J.; Ding, G. YOLOv10: Real-Time End-to-End Object Detection. In Proceedings of the Proceedings of the 38th International Conference on Neural Information Processing Systems, Red Hook, NY, USA, 2025; Vol. 37, *NIPS '24*, pp. 107984–108011.
41. Khanam, R.; Hussain, M. YOLOv11: An Overview of the Key Architectural Enhancements, 2024, [[arXiv:cs/2410.17725](https://arxiv.org/abs/2410.17725)].
42. Meng, D.; Chen, X.; Fan, Z.; Zeng, G.; Li, H.; Yuan, Y.; Sun, L.; Wang, J. Conditional DETR for Fast Training Convergence, 2023, [[arXiv:cs/2108.06152](https://arxiv.org/abs/2108.06152)].
43. Carion, N.; Massa, F.; Synnaeve, G.; Usunier, N.; Kirillov, A.; Zagoruyko, S. End-to-End Object Detection with Transformers. In *Computer Vision – ECCV 2020*; Vedaldi, A.; Bischof, H.; Brox, T.; Frahm, J.M., Eds.; Springer International Publishing: Cham, 2020; Vol. 12346, pp. 213–229.
44. Lin, T.Y.; Goyal, P.; Girshick, R.; He, K.; Dollár, P. Focal Loss for Dense Object Detection, 2018, [[arXiv:cs/1708.02002](https://arxiv.org/abs/1708.02002)].
45. Zhang, H.; Li, F.; Liu, S.; Zhang, L.; Su, H.; Zhu, J.; Ni, L.; Shum, H.Y. DINO: DETR with Improved DeNoising Anchor Boxes for End-to-End Object Detection. In Proceedings of the The Eleventh International Conference on Learning Representations, 2022.
46. Zhang, Y.; Ye, M.; Zhu, G.; Liu, Y.; Guo, P.; Yan, J. FFCA-YOLO for Small Object Detection in Remote Sensing Images. *IEEE Trans. Geosci. Remote Sensing* **2024**, *62*, 1–15.
47. Meng, D.; Chen, X.; Fan, Z.; Zeng, G.; Li, H.; Yuan, Y.; Sun, L.; Wang, J. Conditional DETR for Fast Training Convergence. In Proceedings of the 2021 IEEE/CVF International Conference on Computer Vision (ICCV), Montreal, QC, Canada, 2021; pp. 3631–3640.
48. Tian, Y.; Ye, Q.; Doermann, D. YOLOv12: Attention-Centric Real-Time Object Detectors, 2025, [[arXiv:cs/2502.12524](https://arxiv.org/abs/2502.12524)].

49. Lei, M.; Li, S.; Wu, Y.; Hu, H.; Zhou, Y.; Zheng, X.; Ding, G.; Du, S.; Wu, Z.; Gao, Y. YOLOv13: Real-Time Object Detection with Hypergraph-Enhanced Adaptive Visual Perception, 2025, [[arXiv:cs/2506.17733](https://arxiv.org/abs/2506.17733)].
50. Ge, Z.; Liu, S.; Wang, F.; Li, Z.; Sun, J. YOLOX: Exceeding YOLO Series in 2021, 2021, [[arXiv:cs/2107.08430](https://arxiv.org/abs/2107.08430)].
51. Zhang, S.; Chi, C.; Yao, Y.; Lei, Z.; Li, S.Z. Bridging the Gap Between Anchor-based and Anchor-free Detection via Adaptive Training Sample Selection Between Anchor-Based and Anchor-Free Detection via Adaptive Training Sample Selection. In Proceedings of the Proceedings of the IEEE/CVF Conference on Computer Vision and Pattern Recognition, 2020, pp. 9759–9768.
52. Cai, Z.; Vasconcelos, N. Cascade R-CNN: High Quality Object Detection and Instance Segmentation. *IEEE Transactions on Pattern Analysis and Machine Intelligence* **2021**, *43*, 1483–1498.
53. Peng, Y.; Li, H.; Wu, P.; Zhang, Y.; Sun, X.; Wu, F. D-FINE: Redefine Regression Task in DETRs as Fine-grained Distribution Refinement, 2024, [[arXiv:cs/2410.13842](https://arxiv.org/abs/2410.13842)].
54. Ren, S.; He, K.; Girshick, R.; Sun, J. Faster R-CNN: Towards Real-Time Object Detection with Region Proposal Networks. In Proceedings of the Advances in Neural Information Processing Systems. Curran Associates, Inc., 2015, Vol. 28.
55. Xiao, Y.; Xu, T.; Xin, Y.; Li, J. FBRT-YOLO: Faster and Better for Real-Time Aerial Image Detection.
56. Lyu, C.; Zhang, W.; Huang, H.; Zhou, Y.; Wang, Y.; Liu, Y.; Zhang, S.; Chen, K. RTMDet: An Empirical Study of Designing Real-Time Object Detectors, 2022, [[arXiv:cs/2212.07784](https://arxiv.org/abs/2212.07784)].
57. Feng, C.; Zhong, Y.; Gao, Y.; Scott, M.R.; Huang, W. TOOD: Task-aligned One-stage Object Detection. In Proceedings of the 2021 IEEE/CVF International Conference on Computer Vision (ICCV), Montreal, QC, Canada, 2021; pp. 3490–3499.

Disclaimer/Publisher’s Note: The statements, opinions and data contained in all publications are solely those of the individual author(s) and contributor(s) and not of MDPI and/or the editor(s). MDPI and/or the editor(s) disclaim responsibility for any injury to people or property resulting from any ideas, methods, instructions or products referred to in the content.